# Model-based Variable Impedance Control of Active-Passive Upper-Limb Exoskeleton Assistance and Vibration Attenuation

Yuntian Wang[1] and John McPhee[1]

***Abstract*—This paper proposes a model-based vibration attenuation method for variable-impedance control of a 1-degree-of-freedom active-passive upper-limb exoskeleton. Static and dynamic human efforts are compensated separately, the variable-impedance profile follows a standard law, and the attenuator is derived from identified structural elasticity. To evaluate human adaptation, motor learning was combined with muscle torque generator models. For raising/lowering a weight under the tested conditions, adaptation simulations and a set of human-in-the-loop experiments on one subject show reduced vibration with attenuation; simulations and another set of sEMG-based human-in-the-loop experiments on ten subjects suggest that variable impedance lowers human effort, although motor and human torques are not always aligned.**

***Index Terms*—Prosthetics and Exoskeletons, Compliance and Impedance Control, Modelling and Simulating Humans.**

## I. Introduction

Exoskeletons (EXOs) assist users in power augmentation, yet many devices still hinder motion and increase human effort [1]. An active-passive EXO was designed to combine the benefits of motor and spring assistance [2]. Surface electromyography-based (sEMG) control is sensitive to probe placement and unsuitable for factory use, while force/torque sensors add cost and depend on reliable contact [3]. This study therefore pursues a model-based controller [4] of this active-passive platform. It measures only speed and position data to calculate human torque and ultimately assistance torque by the model.

Model-based control needs an accurate model but avoids sensitive hardware. Human torque can be estimated with disturbance observers (DOB) [4], generalized momentum (GM) [5], and related methods that avoid direct differentiation for acceleration estimation. For this 1-DOF application, these methods reduce to a first-order filter of inverse-dynamics output, so a first-order filter is used.

Upper-limb intent is often non-repetitive, so to cooperate with human intention, prior work uses sEMG [2], proportional control [6], and impedance control with or without prediction [4], [7]. Because impedance generalizes proportional control and high-speed intent prediction can be unreliable, this study focuses on impedance control without prediction. Impedance control can be implemented along a spectrum [8]. Admittance control and “Impedance Control with Computed-Torque” (IC-CT) lie near opposite ends. Compared to IC-CT, admittance control tracks desired impedance more accurately in free space but tends to vibrate in stiff environments, including the studied system. Hence, the more stable IC-CT method was chosen.

Furthermore, variable impedance improves comfort and coordination [9]. Generally, a robot should assist during acceleration and resist otherwise [10]. Hence, Han et al. [9] correlated desired damping to human power to reduce human work, and Hamad et al. [10] used a fuzzy logic scheme to identify human motion phase and change impedance.

Long support chains in shoulder EXOs make low-impedance model-based control prone to vibration: quick stops yield elastic snapbacks that the motor amplifies. To reduce snapback, frequency-based detection with increased desired damping [9] performs poorly under delay, and feedforward compensation [11] struggles because the resonance is in the human motion band (Section III-F). This study proposes attenuation of estimated human torque using a model-based index that dominates only if necessary.

To evaluate the proposed vibration attenuation (VA) and the combined effect of variable impedance control during human-robot interaction, motor learning (Franklin Model) [12] was combined with muscle torque generator (MTG) models [13], forming a new human adaptation model (CNS-MTG). The MTG was used because it expresses excitation (more indicative of effort than activation in the Franklin Model), considers muscle passive torque, and approximates complex joint actuation in 1-DOF settings [13]. To the authors’ knowledge, no prior study has used an antagonistic-muscle adaptation model to evaluate the human-robot interaction. The controllers were also evaluated by sEMG-based human-in-the-loop experiments.

This study developed and assessed control for an active-passive EXO. The main contributions are:

1) A model-based vibration attenuation method for impedance control.
2) A set of 1-DOF human adaptation simulations and sEMG-based human-in-the-loop experiments to assess the effectiveness of vibration-attenuated variable impedance control.

## II. Equipment

The same hardware as [2], [14] was used, except that an extra IMU (Arduino Nano 33 BLE) was attached to the EXO to measure glenohumeral (GH) elevation velocity [15] (Fig. 1b). The Ekso EVO (Ekso Bionics Holdings Inc., California, USA) passive mechanism was augmented in parallel with an AK80-9 KV100 motor (CubeMars Co., Nanchang, China)

Manuscript received: January 21, 2026; Revised May 8, 2026; Accepted July 21, 2026.

This paper was recommended for publication by Editor Pietro Valdastri upon evaluation of the Associate Editor and Reviewers comments.

[1]Yuntian Wang and John McPhee are with the Motion Research Group, Department of System Design Engineering, University of Waterloo, Waterloo, Ontario, N2L 3G1, Canada y3544wan@uwaterloo.ca and mcphee@uwaterloo.ca

Digital Object Identifier (DOI): see top of this page.

This article has been accepted for publication in IEEE Robotics and Automation Letters. This is the author's version which has not been fully edited and content may change prior to final publication. Citation information: DOI 10.1109/LRA.2026.3726343



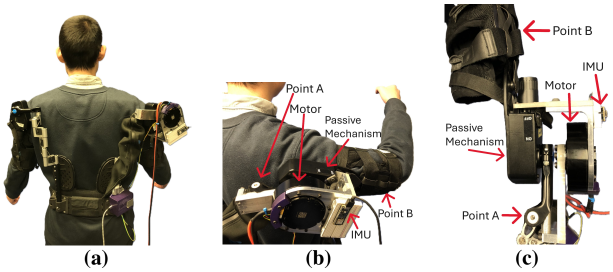


Fig. 1. Active-passive EXO. (a) Back view. (b) Side view. (c) Top view.

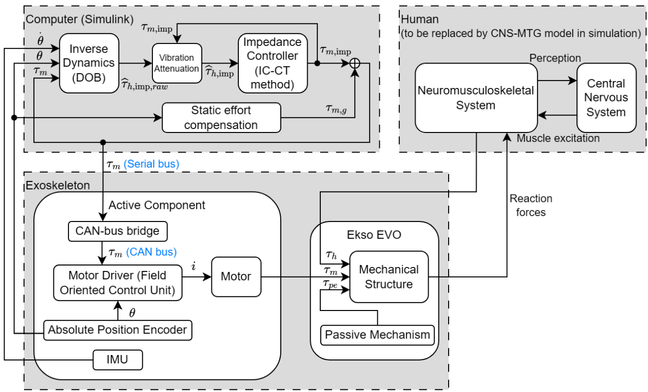


Fig. 2. System flowchart.

and driven by Simulink Desktop Real-Time [16] through a serial bus and an intermediate controller area network (CAN) converter. Only the right EXO tower was modified.

## III. Control Design

A control-oriented human-EXO model was first built (Section III-A) to design a variable impedance controller (Section III-C). Because structural flexibility induces vibration for the impedance controller, an elasticity model was built (Section III-D), identified (Section III-F), and used to design a vibration attenuation method (Section III-G). The unilateral contact constraint was also discussed (Section III-E). The signal flow between the human, EXO, and computer is shown in Fig. 2.

### A. Control-Oriented Human-Exoskeleton Model

The following assumptions are made: the human and EXO body segments are rigid; the plane formed by the points GH (glenohumeral rotation center [15]), elbow joint (center of medial and lateral epicondyle [15]), and hand is parallel to gravity (Fig. 3a); and elbow speed is negligible. Hence, Coriolis and centrifugal terms are neglected, and the arm is modelled as a single pendulum (Eq. 1) with elevation angle $\theta$ in radians (Fig. 3a). Parameters are taken from [14].

$$\tau_m + \tau_h + \tau_{pe} = J_{total}\ddot{\theta} + \tau_f + M_g \tag{1}$$

Here, the variables are defined as:

$$J_{total} = J_{exo} + J_h + m_{ext} l_3^2 \tag{2}$$

$$J_h = m_{ua} l_{uac}^2 + J_{ua} + m_{fa} l_{fac}^2 + J_{fa} \tag{3}$$

$$J_{exo} = N^2 J_m + J_{mech} \tag{4}$$

$$\tau_f = b_{total}\dot{\theta} + M_f \tanh(k_{tanh}\dot{\theta}) \tag{5}$$

$$M_g = M_{g,exo} s_{(\theta)} + M_{g,ua} s_{(\theta)} + M_{g,fa} s_{(\theta+\theta_{o1})} + m_{ext} g l_3 s_{(\theta+\theta_{o2})} \tag{6}$$

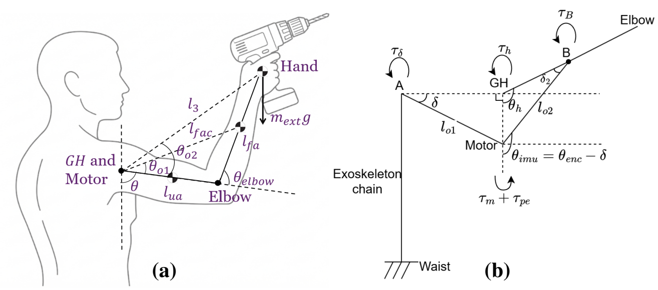


Fig. 3. Human-EXO models. (a) Control-oriented model, where $l_{ua}, l_{fa}$ are upper arm and forearm lengths. Human background generated by Gemini 2.5 Flash Image (Nano Banana) [19]. (b) Elasticity model.

where $s_{(\cdot)}, J, m, ua, fa, l.c, b_{total}$ denotes $\sin(\cdot)$; rotational inertia; mass; upper-arm; forearm; distance-to-mass-center; and the summed viscous friction in the GH joint ($b_h = 0.1$ Nms/rad [14]) and the motor ($b_m$), respectively. Note that the hand segment is combined into the forearm, and $l_3$ is the distance from the elbow joint to the center of mass of the hand. The system is actuated by a motor $\tau_m$ (active actuator assumed to output the exact torque), human muscles $\tau_h$, and a spring-loaded passive mechanism $\tau_{pe}$ (passive actuator), where $\tau_{pe}$ is angle-dependent and was measured by [14]. The assistance torque profile of the level-2 Ekso EVO spring roughly matches the gravitational torque profile of an average male arm [17]:

$$\tau_{pe} = 7.693(-0.45821\theta^2 + 1.90031\theta - 0.9704) \text{ Nm} \tag{7}$$

The system has dynamic (inertia $J_{total}\ddot{\theta}$ and friction $\tau_f$) and static (gravitational torque $M_g$) resistances to be compensated. The total inertia $J_{total}$ consists of the EXO rotating part ($J_{exo}$ of part P10 in [14]), human arm $J_h$, and external load $m_{ext} l_3^2$. The EXO inertia $J_{exo}$ consists of motor rotor inertia $J_m$ and mechanical structures inertia $J_{mech}$. Note that this notation is different from [14]: $J_m$ should be amplified by the motor gear ratio $N = 9$, while the viscous friction $b_m = 0.054$ Nms/rad is defined at the output gear, i.e., it has already been amplified by $N^2$. Friction $\tau_f$ includes viscous and Coulomb-tanh terms [18]. Geometric distances ($l_3$ and $l_{fac}$) and offsets ($\theta_{o1}$ and $\theta_{o2}$) are derived from trigonometry (Fig. 3a).

Maximum gravitational torque of link P10, $M_{g,exo} = 1.0464$ Nm, was measured by a load cell. The weight of forearm ($M_{g,fa}$) and upper arm ($M_{g,ua}$) segments were calculated from anthropometry [17]. Next, it was found that link P10 could keep itself from falling at a certain angle $\theta_{f10}$, so static friction $M_f = M_{exo}\sin(\theta_{f10}) = 0.1745$ Nm. Finally, $J_{exo} = 0.0305$ kg m$^2$ was identified by the free-falling duration of link P10 with the single pendulum model:

$$J_{exo}\ddot{\theta} = -M_{exo}\sin(\theta) - b_m\dot{\theta} - M_f \,\mathrm{sign}(\dot{\theta}) \tag{8}$$

The controller uses $\hat{J}_{total}$ and $\hat{M}_g$ ($\hat{\cdot}$ denotes estimation), with $m_{ext} = 0$, so users can freely change load. To avoid unsafe behavior at negative elevation angles, $\hat{M}_g$ is saturated at zero (Eq. 9).

$$\hat{M}_g = \max(0, M_{g,exo} s_{(\theta)} + M_{g,ua} s_{(\theta)} + M_{g,fa} s_{(\theta+\theta_{o1})}) \tag{9}$$

### B. Human Effort Separation

Fully compensating gravity can hinder downward motion and reduce comfort. A residual gravity component is also needed to preserve scaled load perception. Hence, human and motor torques are separated into static and dynamic components (Eq. 11):

$$\tau_m := \max(0, \tau_{m,imp} + \tau_{m,g}) \tag{10}$$
$$\tau_h := \tau_{h,imp} + \tau_{h,g} \tag{11}$$
$$\tau_{m,g} := \max(0, \Omega\hat{M}_g - \tau_{pe}) \tag{12}$$
$$\tau_{h,g} := (1-\Omega)\hat{M}_g \tag{13}$$

where $\Omega \in [0,1]$ with $\Omega = 0.9$, and $\tau_{m,g}$ is used to complement the gravity portion not covered by $\tau_{pe}$. Substituting Eq. 10-13 into Eq. 1, the following relationship is obtained when saturation is not active:

$$\tau_{m,imp} + \tau_{h,imp} = J_{total}\ddot{\theta} + \tau_f + (M_g - \hat{M}_g) \tag{14}$$

Since the load $m_{ext}$ is unknown, the controller compensates only arm weight; static friction is excluded as well, to reduce vibration:

$$\tau_{m,imp} + \hat{\tau}_{h,imp} := \hat{J}_{total}\ddot{\theta} + \hat{\tau}_f, \text{ where } \hat{\tau}_f := b_{total}\dot{\theta} \tag{15}$$

Using inverse dynamics (Eq. 15), $\hat{\tau}_{h,imp}$ is then estimated, whose result is denoted as $\hat{\tau}_{h,imp,raw}$. Note that the acceleration is estimated by applying the transfer function, $\frac{s}{s/50+1}$ to the measured angular velocity. The term $\tau_{h,imp}$ is to be considered as the external torque in impedance control.

### C. Variable Impedance Control Design

The desired impedance is defined with desired inertia $J_d$ and damping $D_d$:

$$\hat{\tau}_{h,imp} := J_d\ddot{\theta} + D_d\dot{\theta} \tag{16}$$

No target trajectory is used because it is unknown. The implementation follows the IC-CT form in [8]:

$$\begin{aligned}\tau_{m,imp} &= \hat{J}_{total}\ddot{\theta}_d + \hat{\tau}_f - \hat{\tau}_{h,imp}\\ &= \hat{J}_{total}\left(\frac{\hat{\tau}_{h,imp} - D_d\dot{\theta}}{J_d}\right) + b_{total}\dot{\theta} - \hat{\tau}_{h,imp}\\ &= \left(\frac{\hat{J}_{total}}{J_d} - 1\right)\hat{\tau}_{h,imp} + \left(b_{total} - \frac{\hat{J}_{total}D_d}{J_d}\right)\dot{\theta}\end{aligned} \tag{17}$$

For safety, impedance control should be passive, i.e. it dissipates energy injected by the external environment. A desired inertia below half the model inertia can break passivity [20], so $J_d = \hat{J}_{total}/2$ is set. By Landi et al. [21], passivity is guaranteed if $\dot{J}_d < 2D_d$, so enforcing $D_d \geq 0$ is sufficient here. The desired mass significantly affects stability [10] and human perception is more sensitive to damping [22], so only damping is varied around the nominal value $D_{d,nom}$ using a dimensionless scaling factor $K_a(\dot{\theta}, \ddot{\theta}) > 0$ that is close in value to one: $D_d = D_{d,nom}K_a(\dot{\theta}, \ddot{\theta})$.

Three typical variable-impedance profiles are C1, C2, and C3 [10]. For C1, admittance is at the medium value when motion starts, becomes high at the acceleration-deceleration transition, and ends low; profile C3 is similar to C1 but starts low; profile C2 starts medium, peaks in mid-acceleration, returns to medium at the acceleration-deceleration transition, drops in mid-deceleration, and returns to medium at the end. Because only C2 suits agile motions with frequent stops, its typical linear form is used, with $\alpha_+ = 0.05, \alpha_- = 0.05/3$ (named Var-P, Eq. 18). Jerk is excluded due to numerical differentiation noise.

$$K_a(\dot{\theta}, \ddot{\theta}) = \max(0, 1 - \alpha_+ \max(0, \ddot{\theta}\dot{\theta}) - \alpha_- \min(0, \ddot{\theta}\dot{\theta})) \tag{18}$$

### D. Elasticity Model

A preliminary test showed persistent vibration at low impedances. Hence, elasticity is modelled, parameters are identified, and an attenuation method is proposed in this section.

The EXO elasticity is modelled at the right arm (Fig. 3b). The EXO links A-Motor and Motor-B (of lengths $l_{o1}, l_{o2}$ in Fig. 1b), corresponding to the parts P9 and P10 in [14], are assumed parallel to the upper arm GH-Elbow. The motor supports the human arm at the binding point B. The EXO attachment is assumed to provide only an elastic elevation torque $\tau_B$ (Fig. 3b), while preventing radial slipping of the upper arm. The upper-arm skin radius is assumed to be zero.

Elasticity can occur at robot joints and links [23], and the snapback can also be contributed to by motor backlash. Therefore, elasticity is lumped to angular deformation $\delta$ at joint A and $\delta_2$ at binding point B with viscous friction and spring terms (Eq. 22). The IMU on link Motor-B measures the absolute elevation, which deviates from the real human elevation $\theta_{imu} = \theta_h + \delta_2$, while the motor encoder measures $\theta_{enc} = \theta_h + \delta_2 + \delta$. Because of tight binding, $\delta \approx 0$ is assumed. Hence, relating arc length GH-Motor gives:

$$\delta_2 = (l_{o1}/l_{o2})\delta \tag{19}$$
$$\theta_{enc} = \theta_h + (1 + l_{o1}/l_{o2})\delta \tag{20}$$

When $\delta \approx 0$, $\theta_{imu} = \theta_h = \theta_{enc} := \theta$ and $\cos(\delta) \approx 1$. The dynamics of link A-Motor follow:

$$\tau_{m,load} = \tau_m - (N^2 J_m\ddot{\theta}_{enc} + b_m\dot{\theta}_{enc}) \tag{21}$$
$$\tau_\delta = k_\delta\delta + b_\delta\dot{\delta} \tag{22}$$
$$M_{g,o1}\cos(\delta) + \tau_{m,load} + \tau_{pe} = J_{o1}\ddot{\delta} + \tau_\delta \tag{23}$$

where $k_\delta, b_\delta, J_{o1}, \tau_{m,load}, M_{g,o1}$ are rotational stiffness, rotational viscosity, combined moment of inertia of the link A-Motor and the motor rotor, load-side motor torque (applies to the link A-Motor), and gravitational torque on the link A-Motor, respectively. Finally, angle relationship Eq. 20, motor dynamics Eq. 21, and elasticity Eq. 23 yield:

$$\begin{aligned}&\left(J_{o1} + N^2 J_m(1 + l_{o1}/l_{o2})\right)\ddot{\delta} + \left(b_\delta + N^2 b_m(1 + l_{o1}/l_{o2})\right)\dot{\delta}\\ &+ k_\delta\delta = \tau_m + M_{g,o1} + \tau_{pe} - (N^2 J_m\ddot{\theta}_h + b_m\dot{\theta}_h)\end{aligned} \tag{24}$$

Note that elastic torque at point B, $\tau_B$, is not used, due to use of small-angle approximation.

The nonlinear terms ($\tau_{m,g}, M_{g,o1}, \tau_{pe}$) vary relatively slowly and $\theta_h$ is unobservable, so only the linear contribution of $\Delta\tau_{m,imp}$ is considered, with addition of a motor-command delay $T_d$:

$$G_1(s) := \frac{\Delta\delta}{\Delta\tau_{m,imp}} = \frac{\exp(-T_d s)}{\left(J_{o1} + N^2 J_m\left(1 + \frac{l_{o1}}{l_{o2}}\right)\right)s^2 + \left(b_\delta + N^2 b_m\left(1 + \frac{l_{o1}}{l_{o2}}\right)\right)s + k_\delta} \tag{25}$$

For practical use of attenuation, the input and output are modified. The input is replaced by a high-pass-filtered signal, $\tau_{m,imp,f} := \frac{s}{s+10}\tau_{m,imp} \approx \Delta\tau_{m,imp}$, because vibration is mainly excited by high-frequency content. The term $\Delta\dot{\delta}/s$ is also preferred over the drifting $\Delta\delta$. The final elasticity model is:

$$G_2(s) := \frac{\Delta\dot{\delta}}{\tau_{m,imp,f}} \approx (s+10)G_1(s) \tag{26}$$

### E. Unilateral Contact Constraint

Because the human-EXO contact is unilateral, maintaining contact requires the interaction torque $\tau_i > 0$. A simple interaction model is assumed, with $\delta = 0$ and fixed elbow angles,

$$\tau_h + \tau_i = (J_h + m_{ext} l_3^2)\ddot{\theta}_h + b_h \dot{\theta}_h + M_{g,ua} s_{(\theta)} + M_{g,fa} s_{(\theta+\theta_{o1})} + m_{ext} g l_3 s_{(\theta+\theta_{o2})} \tag{27}$$

$$\tau_m + \tau_{pe} - \tau_i = J_{exo} \ddot{\theta}_{imu} + b_m \dot{\theta}_{imu} + M_{g,exo} s_{(\theta_{imu})} \tag{28}$$

An approximately sufficient condition is $\tau_m > 0$. It satisfies $\tau_m > M_{g,exo} s_{(\theta)} - \tau_{pe}$, so Eq. 28 yields $\tau_i > 0$ when $\ddot{\theta}_{imu}$ and $\dot{\theta}_{imu}$ are small.

### F. Elasticity Identification

Several experiments were performed to identify $G_2(s)$. A human wore the EXO with the upper arm fixed to the table, and the Ekso EVO passive mechanism enabled, so elastic deformation was driven only by motor-command changes. The controller ran at 200 Hz. The IMU measured motor speed, and the motor encoder measured position. The nominal model was set from Eq. 26:

$$G_{2,nom}(s) := \frac{\exp(-T_d s)(1 + T_z s) K_p}{1 + 2\zeta T_w s + (T_w s)^2} \tag{29}$$

In experiment 1 (Exp-1), six step-input torque tests (command (a,b) changes from a to b Nm: (1,2), (1,3), (2,3), (2,4), (3,2), (4,2)) estimated delay and gain: $T_d = 0.0936$ s, $K_p = 0.05293$ rad/(Nm s) (standard deviations: 0.0271 s and 0.023 rad/(Nm s)). In experiment 2 (Exp-2), a chirp signal was commanded (4.5-15 Hz over 20 s, 2 Nm bias, 1 Nm amplitude). With these data, the MATLAB System Identification Toolbox [24] estimated Model-1: $K_p = 0.026714$ rad/(Nm s), $T_w = 0.033798$ s, $\zeta = 0.1815$, $T_d = 0.093592$ s, $T_z = 0.105$ s, under constraints: $T_z \in [0.095\ \text{s}, 0.105\ \text{s}]$, $T_d \in [0.0935\ \text{s}, 0.0936\ \text{s}]$, $K_p \in [0, \infty)$ rad/(Nm s), $\zeta \in [0, 1]$. The normalized root mean square error (NRMSE) fit is 38% and the Pearson correlation coefficient between the absolute values $\rho_{|x|,|y|} = 0.76$ (Fig. 4).

In experiment 3 (Exp-3), a sine input (1.5 Hz, 2.5 Nm bias, 1 Nm amplitude) was commanded to validate the model, where Model-1 achieved 45% NRMSE and $\rho_{|x|,|y|} = 0.75$ (Fig. 5) and captured amplitude trends adequately. A separate fit on Exp-3 and Exp-1 data produced Model-2 (48% NRMSE, $\rho_{|x|,|y|} = 0.61$, $K_p = 0.039148$ rad/(Nm s), $T_w = 0.052764$ s, $\zeta = 0.28716$, $T_d = 0.093599$ s, $T_z = 0.093244$ s), which is used to inject modelling error in simulations. The rest of the paper refers to Model-1 unless noted otherwise. Since VA uses only the estimated vibration-amplitude trend of $\dot{\delta}$ (Section III-G), the correlation values $\rho_{|x|,|y|} = 0.76, 0.75$ are deemed as sufficient.

### G. Vibration Attenuation and Passivity

The identified $G_2(s)$ resonates at 4.76 Hz with a peak gain of -12.4 dB, within the common human force-control bandwidth (5-10 Hz [25]); thus its resonance cannot be separated from the human voluntary motion. Hence, the estimated human torque is proposed to be directly attenuated when a vibration index is high. First, $\tau_m$ (or $\tau_{m,imp}$) is high-pass filtered by $s/(s+10)$ and fed into the elasticity model $G_2(s)/\exp(-T_d s)$ (delay ignored) to get $\dot{\delta}$. Next, the absolute-value function and a low-pass filter $1/(0.4s+1)$ are applied to obtain a smooth index $\delta_{id}$, approximating the vibration amplitude. Finally, vibration attenuation (VA) is achieved:

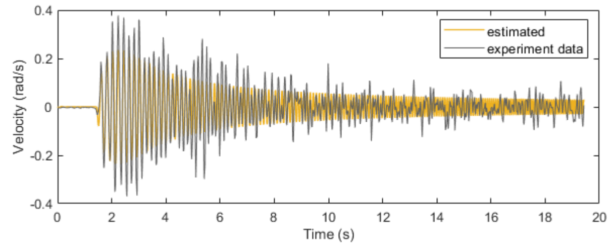


Fig. 4. Model-1 fit result for chirp input.

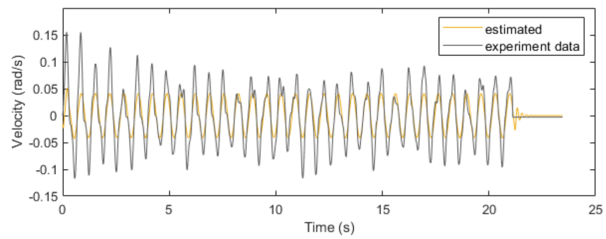


Fig. 5. Model-1 fit result for sine input.

$$\hat{\tau}_{h,imp} = \hat{\tau}_{h,imp,raw} K_{decay,2} \exp\left(-\frac{\delta_{id} K_{decay,1}}{|\dot{\theta}| + \varepsilon}\right) := \hat{\tau}_{h,imp,raw} G_3 \tag{30}$$

where $\varepsilon = 0.05$ rad/s avoids zero division, $K_{decay,1}, K_{decay,2} > 0$ are constant decay rates, and $G_3(\delta_{id}, \dot{\theta}) \in (0, 1]$ is the attenuation gain.

As noted in Section III-C, variable-impedance passivity (Eq. 16) is guaranteed if $D_d \geq 0$. The analysis below shows that elasticity can violate passivity, but the proposed VA method can retain the passivity when $\tau_{h,imp}\dot{\theta} \geq 0$ and maintain asymptotic stability when $\tau_{h,imp}\dot{\theta} < 0$. Consider a positive definite and proper energy storage (Lyapunov) function $V(\theta, \tau_{h,imp}) = (J_d \dot{\theta}^2)/2$ and Eq. 16,

$$\dot{V} = J_d \ddot{\theta}\dot{\theta} = \hat{\tau}_{h,imp}\dot{\theta} - D_d \dot{\theta}^2 \leq \hat{\tau}_{h,imp}\dot{\theta} \tag{31}$$

Suppose there are no unmodelled uncertainties; from inverse dynamics, the estimated torque $\hat{\tau}_{h,imp,raw}$ (calculated using $\theta_{enc}$, Eq. 20) is related to the true value (calculated using $\theta_h$) by Eq. 32, which leads to Eq. 33:

$$\hat{\tau}_{h,imp,raw} = \tau_{h,imp} + J_{total}(1 + l_{o1}/l_{o2})\ddot{\delta} \tag{32}$$

$$\dot{V} = (\tau_{h,imp} + J_{total}(1 + l_{o1}/l_{o2})\ddot{\delta}) G_3 \dot{\theta} - D_d \dot{\theta}^2 \tag{33}$$

If the gain $G_3 > 0$ is designed such that,

$$\forall t, J_{total}(1 + l_{o1}/l_{o2})|\ddot{\delta}| G_3 \leq D_d |\dot{\theta}| \tag{34}$$

the passivity condition ($\dot{V} \leq \tau_{h,imp}\dot{\theta}$) would be satisfied when $\tau_{h,imp}\dot{\theta} \geq 0$. When $\tau_{h,imp}\dot{\theta} < 0$, the passivity is not guaranteed. However, if Eq. 34 holds, $\dot{V} < 0$, and the origin $\dot{\theta} = 0$ would be asymptotically stable by the Lyapunov's direct method. The condition (Eq. 34) implies that the proposed $G_3$ gain (Eq. 30) should increase with $|\dot{\theta}|$ and decrease with $|\ddot{\delta}|$, which can be arbitrarily satisfied by tuning $K_{decay,1}, K_{decay,2}$. Since $\delta_{id}$ correlates with the vibration amplitude of $\dot{\delta}$, it correlates implicitly with $|\ddot{\delta}|$. Without VA, $G_3 = 1$, and $\dot{V}$ can become positive, making the system unstable.

## IV. Human-Exoskeleton Adaptation Simulation

A MATLAB simulation was built to assess the proposed VA method and variable impedance control, and to evaluate human adaptation. The system follows Section III-A and III-D, with $m_{ext} = 0.25$ kg and fully extended elbow. Human body segment inertial parameters were scaled from an average adult male (1.77 m height; 27.5 years old; and 80.5 kg mass) [17] to the subject (male; 1.73 m height; 25 years old; 64.29 kg mass; right-handed; workout frequency: 7/week).

### A. Human Adaptation Model

A motor learning model (Franklin model) [12] was combined with an MTG model, to act as the human model (CNS-MTG model). The MTG enables reporting muscle excitation instead of activation, which better reflects effort [13].

*1) Franklin Model:* The net muscle force $\vec{F}_{total}$ generated by an antagonistic muscle pair is [12],

$$\vec{F}_{total} = \max(0, F^+ + (\kappa_0 + \kappa_1 F^+)(e_\lambda + \kappa_d \dot{e}_\lambda))\hat{r}^+ - \max(0, F^- + (\kappa_0 + \kappa_1 F^-)(-e_\lambda - \kappa_d \dot{e}_\lambda))\hat{r}^- \quad (35)$$

It assumes adaptation toward an internal planned trajectory. Given a flexor muscle activation $F^+$, tracking uses varying muscle impedance $\kappa_0 + \kappa_1 F^+$, and similarly for the extensor muscle activation $F^-$. Here, $e_\lambda(t)$ and $\dot{e}_\lambda(t)$ are muscle-length position and velocity tracking errors at time $t$; $\kappa_0, \kappa_1, \kappa_d > 0$ are constants; and unit vectors $\hat{r}$ denote force directions. Superscripts $^+, ^-$ denote flexor and extensor muscles throughout this paper.

Humans adjust the activation $F^+$ to improve tracking, which consists of feedforward, feedback, and noise parts (Eq. 36). The noise part depends on the feedforward (Eq. 37).

$$F^+ = \max(0, F^+_{FF} + F^+_{noise} + F^+_{FB}) \quad (36)$$

$$F^+_{noise}(t) = (\mu_0 + \mu_1 F^+_{FF}(t))\mu(t) \quad (37)$$

where $\mu(t) = 12.5 f(\nu(t))$, parameters $\mu_0, \mu_1 > 0$, and $f(\cdot)$ is a causal fifth-order Butterworth filter with 2 Hz cut-off frequency. The random variable $\nu(t) \in \mathcal{N}(0,1)$ is normally distributed. The feedback part $F^+_{FB}(t)$ is adjusted online towards the planned trajectory, with a feedback delay $\psi > 0$ and feedback gains $r, r_d > 0$:

$$F^+_{FB}(t) = r(e_\lambda(t-\psi) + r_d \dot{e}_\lambda(t-\psi)) \quad (38)$$

where $F^+_{FB}(t)$ can be positive or negative. The feedforward is updated trial-by-trial from the last trial error. The flexor update rule follows Eq. 39, and the same applies to the extensor:

$$F^{+,k+1}_{FF}(t) = \max(0, F^{+,k}_{FF}(t) + \Delta F^{+,k}_{FF}(t+\psi)) \quad (39)$$

where,

$$\Delta F^{+,k}_{FF}(t+\psi) = \alpha |e^k(t)| I_{\{e^k(t)\geq 0\}} + \beta |e^k(t)| I_{\{e^k(t)<0\}} - \gamma \quad (40)$$

$$e^k = e^k_\lambda + g_d \dot{e}^k_\lambda \quad (41)$$

Here, $I_{\{S\}}$ is the Kronecker function (1 if statement S is true, else 0). The superscript $^k$ denotes trial index. Parameters $\alpha, \beta, \gamma, g_d$ are positive constants with $\alpha > \beta$. Ideally, adaptation transfers effort from feedback to feedforward. Agonist and antagonist feedforward efforts adapt together: they initially increase at different rates in a new dynamic environment (dominated by $\alpha, \beta$), then decrease and converge when the $-\gamma$ term balances the others. Refer to [12] for more details.

*2) CNS-MTG Model:* The net joint torque $\tau_{total}$ generated by the antagonistic muscle pair is,

$$\tau_{total} = \tau^+_a - \tau^-_a + \tau_p \quad (42)$$

$$\tau^+_a = \mathrm{sat}(\tau^+_{a1} + (\kappa'_0 + \kappa'_1 \tau^+_{a1})(e_\theta + \kappa_d \dot{e}_\theta), 0, \tau^+_{max}) \quad (43)$$

$$\tau^-_a = \mathrm{sat}(\tau^-_{a1} + (\kappa'_0 + \kappa'_1 \tau^-_{a1})(-e_\theta - \kappa_d \dot{e}_\theta), 0, \tau^-_{max}) \quad (44)$$

where $_a$ denotes activation, $'$ denotes the scaled version of parameters in [12], $\tau_p(\theta, \dot{\theta})$ is passive torque from [13], and the muscle-length error $e_\lambda(t)$ [12] has been converted to joint-angle error $e_\theta(t)$. For the flexor muscle,

$$\tau^+_{max} := \tau^+_\omega \tau^+_\theta \tau^+_0 \quad (45)$$

$$\tau^+_e = \mathrm{sat}(\tau^+_{FF} + \tau^+_{noise} + \tau^+_{FB}, 0, \tau^+_{max}) := u^+_{ex} \tau^+_{max} \quad (46)$$

$$\tau^+_{a1} = \tau^+_{e2a}(\tau^+_e, t) := u^+_{act} \tau^+_{max} \quad (47)$$

where $\tau_\omega(\dot{\theta}), \tau_\theta(\theta), \tau_0, \tau_{max}(\theta, \dot{\theta}), \tau^+_{e2a}(\tau^+_e, t)$ denote active-torque-speed scaling, active-torque-angle scaling, peak joint strength, the maximum generatable torque, and excitation-to-activation mapping, respectively [13]. The saturation operator is $\mathrm{sat}(x,a,b) := \min(\max(x,a),b)$. The excitation torque profile $\tau_e(t)$ is updated trial-by-trial to follow the planned trajectory, and then the muscle effort $u_{ex}(t) = \tau_e(t)/\tau^+_{max}$ is reported. The normalized signals $u_{ex}, u_{act} \in [0,1]$ are the normalized versions of $\tau_a, \tau_e \in [0, \tau_{max}]$. Next, the noise, feedback, and feedforward components are:

$$\tau^+_{noise}(t) = (\mu_0 + \mu_1 \tau^+_{FF}(t))\mu(t) \quad (48)$$

$$\tau^+_{FB}(t) = r'(e_\theta(t-\psi) + r_d \dot{e}_\theta(t-\psi)) \quad (49)$$

$$\tau^{+,k+1}_{FF}(t) = \mathrm{sat}(\tau^{+,k}_{FF}(t) + \Delta\tau^{+,k}_{FF}(t+\psi), 0, \tau^+_{max}(t)) \quad (50)$$

The modified update part is,

$$\Delta\tau^{+,k}_{FF}(t+\psi) = \alpha' |e'^k(t)| I_{\{e'^k(t)\geq 0\}} + \beta' |e'^k(t)| I_{\{e'^k(t)<0\}} - \gamma' \quad (51)$$

$$e'^k = e^k_\theta + g_d \dot{e}^k_\theta \quad (52)$$

An approximately constant slope was found between the deltoid anterior fiber length and the humerus flexion angle for sagittal flexion from 0° to 90° using the OpenSim model [26]. From 50 uniformly sampled points, the mean slope is 28.42 rad/m (standard deviation 5.60 rad/m). Therefore, the constant ratio $\rho_{l2a} = 28.42$ rad/m is defined and converts the parameters: $\kappa'_0 = \kappa_0 \rho_s/\rho_{l2a}$, $\kappa'_1 = \kappa_1/\rho_{l2a}$, $\alpha' = \alpha\rho_s/\rho_{l2a}$, $\beta' = \beta\rho_s/\rho_{l2a}$, $r' = r\rho_s/\rho_{l2a}$, $\gamma' = \gamma\rho_s$, where the angular scaling assumes constant shoulder-elevation moment arm $\rho_s = \rho^+_s = \rho^-_s = 0.03$ m as in [12].

### B. Simulation Configurations

Using the CNS-MTG model (Section IV-A2), system dynamics (Section III-A), and elasticity model (Section III-D), sagittal up motions (from 48.1° to 87.7°) and down motions (from 89.7° to 48.1°) were simulated, with time discretization at 200 Hz. Target trajectories were recorded from a healthy subject wearing the EXO with all actuators ($\tau_{pe}, \tau_m$) off and no external hand load. The up and down motion profiles were selected to be approximately symmetric, each with 0.75 s rest, 0.75 s motion, and 0.75 s rest.

The plant has the elastic behaviour implemented by the transfer function of Model-2, while the controller uses elasticity Model-1 for attenuation (defined in Section III-F). The controller observes $\hat{\dot{\theta}} = \dot{\theta}_{imu}$ and $\hat{\theta} = \theta_{enc}$.

Tests were simulated with the following configurations:

This article has been accepted for publication in IEEE Robotics and Automation Letters. This is the author's version which has not been fully edited and content may change prior to final publication. Citation information: DOI 10.1109/LRA.2026.3726343



0) Human only (not wearing EXO).
1) Fixed impedance. **a**) VA disabled ($D_d = 0.5b_{total}$). **b**) VA enabled ($D_d = 0.5b_{total}$). **c**) VA disabled ($D_d = 10b_{total}$).
2) Fixed impedance ($D_d = 4.5b_{total}$); VA enabled.
3) Var-P $\left(D_{d,nom} = 4.5b_{total}\right)$; VA enabled.

The human feedforward excitations were first adapted from zero in TEST 0 for 200 trials, then separately adapted for EXO assistance cases (TEST 1-3) for 200 trials each.

Abnormal adaptation behavior was observed, especially in the down-motion, after saturation of $\tau_{FF}^{+,k}(t)$ or $\tau_{FF}^{-,k}(t)$ at time $t$: when one saturates, the other keeps increasing and no equilibrium is reached. To mitigate it, $\tau_{FF}^{-} = 0$ is assumed for TEST 0. This is valid because: **(i)** The antagonist muscle feedforward level can be reduced to zero after adaptation [27], given the agonist muscle activity is not extremely large [28] and there is no external perturbation. **(ii)** The user must have adapted to the TEST 0 condition for years. **(iii)** The arm acts against the gravity, whose effect outweighs that of the acceleration demand. **(iv)** The adaptation result yield $\forall t, \tau_{FF}^{+} > 0$, using the assumption. **(v)** The same adaptation results are obtained for the up-motion with or without the assumption. Accordingly, for TEST 0 only, the flexor/extensor update rules (Eq. 52) were replaced by Eq. 53 and 54. The modification is reasonable because with prescribed motion and no coactivation, inverse dynamics yields a unique converged excitation profile.

$$\Delta\tau_{FF}^{+,k}(t+\psi) = \alpha' e'^{k}(t) - \gamma' \tag{53}$$

$$\Delta\tau_{FF}^{-,k}(t+\psi) = 0 \tag{54}$$

The VA method uses $K_{decay,1} = 25$ s/rad$, K_{decay,2} = 1$. Because excitation saturation can cause abnormal adaptation, predefined trajectories were chosen slow enough to avoid it. To better expose VA effects, speed profiles were scaled by 1.5 for TEST 1a-1c to create sudden stops. The saturation does not change adapted torque profiles in these tests, so this is acceptable. TEST 1a-1c are presented to evaluate the VA performance, and they are not meant for deployment, unlike TEST 2 and 3.

### C. Results and Discussion

The proposed VA method significantly reduced vibration (Fig. 6.a1; vibration sustained after 1.1 s; peak-to-peak amplitude 2.09 N m), with minimal effect on the normal assistance: the maximum absolute differences between the attenuated and unattenuated $\tau_{m,imp}$ are 0.68 and 0.89 N m over 0.75-1.35 s in Fig. 6.a1-a2, respectively. The estimated vibration index adequately tracked true amplitude trends (Fig. 6.i1-i2). Note that $\tau_{m,imp}$ is omitted in TEST 1a-1b of Fig. 6.a1-a2, where $\tau_{m,imp} = \tau_{h,imp}$. With a higher damping ($D_d = 10b_{total}$) and VA disabled, vibration in up-motion still persisted at amplitudes similar to TEST 1a (purple lines in Fig. 6.a1-a2).

After 200 trials, all controllers approximately reached target trajectories; Var-P examples are in Fig. 6.e-f. All tested EXO assistance methods (TEST 2 and 3) reduced the muscle fatigue in the up-motion, comparing to the human-only baseline, but not in the down-motion (Fig. 7). The down-motion generally requires less muscle excitation than the up-motion, partly due to the eccentric muscle contraction against gravity [29]. Although the EXO assistance significantly reduced human torque integral in the down-motion (Fig. 7), muscle co-activation increased ($(\sum u_{ex}^{+}\Delta t, \sum u_{ex}^{-}\Delta t)$ data for TEST 0, 2, and 3: (0.13,0), (0.14,0.01), (0.07,0.09)), indicating an unwanted uncertainty added from assistance. This matches human-in-the-loop experimental results in [30]: flexor activity decreases while extensor activity increases with EXO assistance. Notably, the EXO assistance lowered up-motion effort to near down-motion levels.

Three dynamic-performance metrics were evaluated over 0.6-1.65 s (Fig. 7): integral of human torque, integral of antagonistic MTG excitation sum, and correlation between sign($\tau_{h,imp}$) and sign($\tau_{m,imp}$). The static motion periods (0-0.6 s and 1.65-2.25 s) were excluded because the impedance controller output should be zero at zero velocity and acceleration and the static human efforts are obviously reduced by the gravity compensation. The noise observed in 0-0.6 s of Fig. 6.a-c are caused by the initial zero activation; the noise in 1.65-2.25 s are caused by the joint elasticity. In Fig. 7, Var-P leads all the metrics, except that the fixed impedance control is better in the human-torque integral for the down-motion and the MTG-excitation-sum integral for the up-motion. Since all EXO controllers increased down-motion excitation, that tradeoff is more concerning; overall, Var-P is preferable.

Co-activation integrals rose in early adaptation and then declined (Fig. 6.g-h), consistent with [12]. The human-only values are too large to plot in Fig. 6.g-h, but follow the same trend. As expected, the flexor effort exceeds the extensor effort in the up-motion, and the reverse occurs in the down-motion. The Var-P damping profile generally followed human motion intent with limited spikes (Fig. 6.d1-d2).

## V. Human-in-the-loop Experiments

This section presents human-in-the-loop (HITL) experiments to test the VA and impedance control, on the right upper body with fully extended elbow. The University of Waterloo Research Ethics Board approved the study (REB: #43980), and all subjects provided informed consent.

### A. Vibration Attenuation Validation

A HITL experiment assessed VA effectiveness on one healthy subject. One subject was deemed sufficient because the VA effect depends mainly on motion profile, not person. The subject raised the right arm from $\theta = 40°$ to $90°$ with a fast (0.5 s) and a slow (1 s) timing under fixed or Var-P impedance control, with or without VA ($J_d = \hat{J}_{total}/2, D_d = 0.5b_{total}$). The down-motion was also tested but omitted due to similar behaviour.

The position curves show step-like edges (Fig. 8.a-b), due to EXO-joint friction. Without VA, oscillation occurred and persisted when the user attempted to hold the position (peak-to-peak amplitude $A_{p-p} \approx 8.8°$ in Fig. 8.a and $A_{p-p} \approx 4.1°$ in Fig. 8.b). With VA, the vibration was reduced considerably, to a level the subject judged comfortable. The VA also had little effect on the assistance performance when little vibration was present (Fig. 8.a-b).

Fixed impedance control with a higher-damping without VA was also tested. Similar to Fig. 8.a-b, the vibration sometimes

This article has been accepted for publication in IEEE Robotics and Automation Letters. This is the author's version which has not been fully edited and content may change prior to final publication. Citation information: DOI 10.1109/LRA.2026.3726343



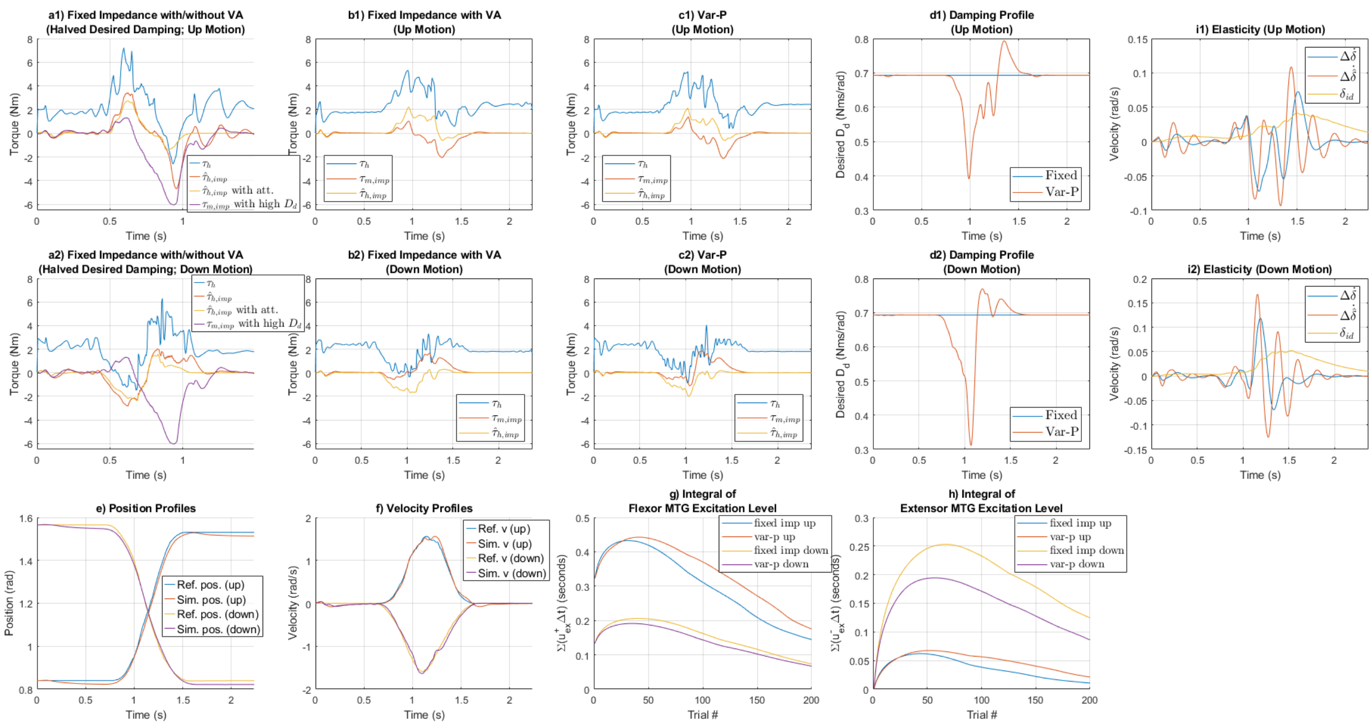


Fig. 6. Simulation adaptation results after 200 trials. (a1-c1) Real human torque, impedance part of motor torque, and estimated impedance part of human torque of up-motion in TEST 1-3. The results of TEST 1a-1c are combined to (a1). (a2-c2) down-motion version of (a1-c1). (d1 & d2) Desired damping profile in TEST 2 and 3 during up (d1) and down (d2) motions. (e & f) Human target motion trajectory compared to simulated motion in TEST 3. (g & h) Integral of flexor $u_{ex}^{+}$ and extensor $u_{ex}^{-}$ muscle excitations in TEST 2 and 3 across adaptation trials. (i1 & i2) Elasticity in TEST 3: true elasticity, estimated elasticity, and estimated elasticity index.

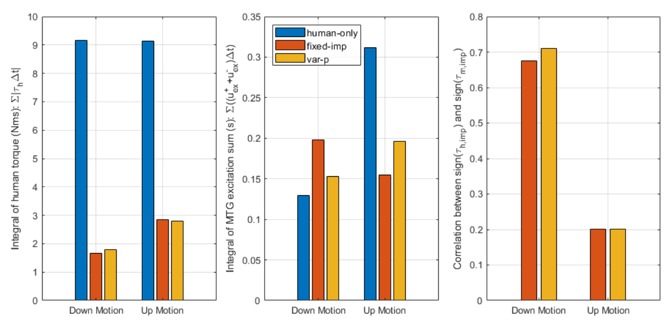


Fig. 7. Metrics evaluated at the 200th trial for TEST 0, 2, and 3.

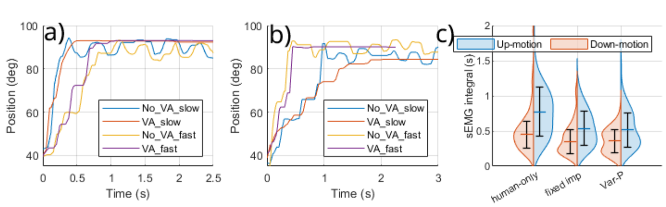


Fig. 8. HITL experimental results. (a & b) VA experiment: position data for (a) the fixed impedance control and (b) the Var-P. (c) sEMG experiments: sum of sEMG integral over five muscles (upper trapezius, middle trapezius, middle deltoid, posterior deltoid, and anterior deltoid [2]). The mean (red line for down-motion, blue line for up-motion) and the standard deviation (black line) are marked on the violin plots of data distributions.

grows to infinity while the user tried to remain still, and the high damping resisted motion. The intensified vibration may be caused by the control delay and numerical differentiation.

### B. sEMG-based Evaluation of Variable Impedance Control

A sEMG-based HITL experiment evaluated the impedance controllers on ten healthy subjects (5 male and 5 female; mean $\pm$ standard deviation: $24.9 \pm 2.2$ years old; $64.6 \pm 6.9$ kg mass; $1.70 \pm 0.09$ m height; $1.4 \pm 1.15$ workout sessions/week; one left-handed; $0.32 \pm 0.03$ m upper-arm length; $0.26 \pm 0.03$ m forearm length). The sEMG hardware and its usage followed [2], except that brachioradialis was excluded as irrelevant. Before testing each subject, $M_{g,ua}$ and $M_{g,fa}$ were scaled by a common gain to fully compensate gravity ($\Omega = 1$) at the horizontal posture.

Three conditions were tested: human-only (no EXO), fixed impedance, and Var-P. For each condition, the subjects performed 10 repeated up-and-down motion cycles (20 trials total) in the sagittal plane with 3 s rest between motions, while seated upright, facing an instruction screen, holding a 5 lb kettlebell, and keeping the elbow and scapula fixed. Subjects were asked to relax the shoulder at the down position; move the arm from down (hand at the knee level) to up (screen mark) as quickly and as stably as possible upon cue on screen, and similarly for the down-motion.

The summed integral of normalized sEMG signals [2] is evaluated over the motion periods (Fig. 8.c), which is defined from the first time the absolute velocity becomes higher than the threshold ($|\dot{\theta}| > 0.1$ rad/s) to the first time it is below the threshold and $\theta$ is within $2.5^{\circ}$ of the final position. An IMU (Arduino Nano 33 BLE) was attached to the upper arm in the human-only test to measure $\theta$ and capture the motion periods. Unlike the simulations, the sEMG integrals showed no clear monotonic trend across trials, suggesting near-instant adaptation. Hence, only 20 trials were tested to limit fatigue carryover for the consecutive tests. However, the resulting effort levels were consistent with the simulation: the down-motion required less effort than the up-motion, and both controllers reduced human effort to similar levels in each direction (Fig. 8.c). The Var-P slightly outperformed the fixed impedance control, reducing sEMG integral by 33% (up) and 20% (down) relative to the human-only case.

## VI. Conclusion and Future Directions

This study investigated power-augmentation strategies for a 1-DOF active-passive EXO [2] that does not rely on sEMG or force/torque sensors. The contributions were achieved through the integration of a variable impedance controller (Var-P) with a novel vibration attenuation (VA) block derived from identified structural elasticity. To evaluate human-robot adaptation, a novel CNS-MTG human model was developed for simulation, coupling motor learning and muscle models. The simulation and one-subject HITL results show that VA effectively reduces vibration without compromising normal assistance under the tested conditions. The simulation and ten-subject HITL results suggest that, under the tested conditions, Var-P slightly outperformed the fixed impedance control, while both significantly reduced up-motion human effort. In the simulation, however, the down-motion muscle effort rises to a level similar to the up-motion under EXO assistance. Future work should assess these controllers on more subjects with more metrics (e.g. metabolic data and subjective assessments), more adaptation trials, and more loads and motion conditions.

## References


[1] W. Cornwall, "In pursuit of the perfect power suit," *Science*, vol. 350, no. 6258, pp. 270–273, Oct. 2015.

[2] A. Nasr, J. Hunter, C. R. Dickerson, and J. McPhee, "Evaluation of a machine-learning-driven active-passive upper-limb exoskeleton robot: Experimental human-in-the-loop study," *Wearable Technologies*, vol. 4, p. e13, 2023.

[3] W. Zou, X. Chen, S. Li, P. Duan, N. Yu, and L. Shi, "Robust admittance control for human arm strength augmentation with guaranteed passivity: A complementary design," *IEEE/ASME Transactions on Mechatronics*, vol. 27, no. 6, pp. 5936–5947, Dec. 2022.

[4] S. Oh and Y. Hori, "Generalized discussion on design of force-sensor-less power assist control," in *2008 10th IEEE International Workshop on Advanced Motion Control*. Trento, Italy: IEEE, Mar. 2008, pp. 492–497.

[5] T. Li, H. Xing, E. Hashemi, H. D. Taghirad, and M. Tavakoli, "A brief survey of observers for disturbance estimation and compensation," *Robotica*, vol. 41, no. 12, pp. 3818–3845, Dec. 2023.

[6] A. Nasr, A. Hashemi, and J. McPhee, "Model-based mid-level regulation for assist-as-needed hierarchical control of wearable robots: A computational study of human-robot adaptation," *Robotics*, vol. 11, no. 1, p. 20, Jan. 2022.

[7] A. Oliveira Souza, J. Grenier, F. Charpillet, S. Ivaldi, and P. Maurice, "Enhancing exoskeleton transparency with motion prediction: An experimental study," in *IEEE-RAS International Conference on Humanoid Robots*, Nancy, France, Nov. 2024.

[8] N. Berezny and M. Ahmadi, "Unifying impedance control, admittance control, and hybrid methods into a sensitivity framework," Jun. 2025.

[9] L. Han, L. Zhao, Y. Huang, and W. Xu, "Variable admittance control for safe physical human-robot interaction considering intuitive human intention," *Mechatronics*, vol. 97, p. 103098, Feb. 2024.

[10] Y. M. Hamad, Y. Aydin, and C. Basdogan, "Adaptive human force scaling via admittance control for physical human-robot interaction," *IEEE Transactions on Haptics*, vol. 14, no. 4, pp. 750–761, Oct. 2021.

[11] G. Solak and A. Ajoudani, "Online learning and suppression of vibration in collaborative robots with power tools," in *2023 IEEE International Conference on Robotics and Automation (ICRA)*, 2023, pp. 12 085–12 091.

[12] D. W. Franklin, E. Burdet, K. Peng Tee, R. Osu, C.-M. Chew, T. E. Milner, and M. Kawato, "CNS learns stable, accurate, and efficient movements using a simple algorithm," *The Journal of Neuroscience*, vol. 28, no. 44, pp. 11 165–11 173, Oct. 2008.

[13] A. Nasr, A. Hashemi, and J. McPhee, "Scalable musculoskeletal model for dynamic simulations of upper body movement," *Computer Methods in Biomechanics and Biomedical Engineering*, vol. 27, no. 3, pp. 306–337, Feb. 2024.

[14] A. Nasr, S. Bell, and J. McPhee, "Optimal design of active-passive shoulder exoskeletons: a computational modeling of human-robot interaction," *Multibody System Dynamics*, vol. 57, no. 1, pp. 73–106, Jan. 2023.

[15] G. Wu, F. C. T. v. d. Helm, H. E. J. D. Veeger, M. Makhsous, P. V. Roy, C. Anglin, J. Nagels, A. R. Karduna, K. McQuade, X. Wang, F. W. Werner, and B. Buchholz, "ISB recommendation on definitions of joint coordinate systems of various joints for the reporting of human joint motion—Part II: shoulder, elbow, wrist and hand," *Journal of Biomechanics*, vol. 38, no. 5, pp. 981–992, 2005.

[16] The MathWorks, Inc., *Simulink Desktop Real-Time*, The MathWorks, Inc., Natick, MA, USA, 2024, version R2024b.

[17] R. Dumas, L. Chèze, and J.-P. Verriest, "Adjustments to McConville et al. and Young et al. body segment inertial parameters," *Journal of Biomechanics*, vol. 40, no. 3, pp. 543–553, Jan. 2007.

[18] S. Andersson, A. Söderberg, and S. Björklund, "Friction models for sliding dry, boundary and mixed lubricated contacts," *Tribology International*, vol. 40, no. 4, pp. 580–587, Apr. 2007.

[19] Google DeepMind, "Gemini 2.5 flash image (nano banana)," 2025, large multimodal model. [Online]. Available: https://ai.google.dev/gemini-api/docs/image-generation

[20] J. E. Colgate and N. Hogan, "Robust control of dynamically interacting systems," *International Journal of Control*, vol. 48, no. 1, pp. 65–88, 1988.

[21] C. T. Landi, F. Ferraguti, L. Sabattini, C. Secchi, and C. Fantuzzi, "Admittance control parameter adaptation for physical human-robot interaction," in *2017 IEEE International Conference on Robotics and Automation (ICRA)*, 2017, pp. 2911–2916.

[22] V. Duchaine and C. M. Gosselin, "General model of human-robot cooperation using a novel velocity based variable impedance control," in *Second Joint EuroHaptics Conference and Symposium on Haptic Interfaces for Virtual Environment and Teleoperator Systems (WHC'07)*. Tsukuba, Japan: IEEE, Mar. 2007, pp. 446–451.

[23] A. De Luca and W. Book, *Robots with Flexible Elements*. Berlin, Heidelberg: Springer Berlin Heidelberg, 2008, pp. 287–319.

[24] I. b. The MathWorks, "System identification toolbox," Natick, Massachusetts, United States. [Online]. Available: https://www.mathworks.com/help/ident/

[25] T. L. Brooks, "Telerobotic response requirements," in *1990 IEEE International Conference on Systems, Man, and Cybernetics Conference Proceedings*. Los Angeles, CA, USA: IEEE, 1990, pp. 113–120.

[26] K. R. Saul, X. Hu, C. M. Goehler, M. E. Vidt, M. Daly, A. Velisar, and W. M. Murray, "Benchmarking of dynamic simulation predictions in two software platforms using an upper limb musculoskeletal model," *Computer Methods in Biomechanics and Biomedical Engineering*, vol. 18, no. 13, pp. 1445–1458, Oct. 2015.

[27] D. W. Franklin, R. Osu, E. Burdet, M. Kawato, and T. E. Milner, "Adaptation to Stable and Unstable Dynamics Achieved By Combined Impedance Control and Inverse Dynamics Model," *Journal of Neurophysiology*, vol. 90, no. 5, pp. 3270–3282, Nov. 2003.

[28] S. Maeo, T. Takahashi, Y. Takai, and H. Kanehisa, "Trainability of Muscular Activity Level during Maximal Voluntary Co-Contraction: Comparison between Bodybuilders and Nonathletes," *PLoS ONE*, vol. 8, no. 11, p. e79486, Nov. 2013.

[29] S. Hody, J.-L. Croisier, T. Bury, B. Rogister, and P. Leprince, "Eccentric Muscle Contractions: Risks and Benefits," *Frontiers in Physiology*, vol. 10, p. 536, May 2019.

[30] M. Musso, A. S. Oliveira, and S. Bai, "Influence of an upper limb exoskeleton on muscle activity during various construction and manufacturing tasks," *Applied Ergonomics*, vol. 114, p. 104158, Jan. 2024.